

Prospects for detecting the Rossiter-McLaughlin effect of Earth-like planets: the test case of TRAPPIST-1b and c

Ryan Cloutier^{1,2,3} & Amaury H. M. J. Triaud⁴

¹*Dept. of Astronomy & Astrophysics, University of Toronto.*

50 St. George Street, Toronto, Ontario, Canada, M5S 3H4

²*Centre for Planetary Sciences, Department of Physical & Environmental Sciences, University of Toronto.*

1265 Military Trail, Toronto, Ontario, Canada, M1C 1A4

³*Institut de recherche sur les exoplanètes, Département de physique, Université de Montréal.*

2900 boul. douard-Montpetit, Montréal Quebec, Canada, H3T 1J4

⁴*Institute of Astronomy, University of Cambridge. Madingley Road, Cambridge CB3 0HA, United Kingdom.*

4 June 2021

ABSTRACT

The Rossiter-McLaughlin effect is the principal method of determining the sky-projected spin-orbit angle (β) of transiting planets. Taking the example of the recently discovered TRAPPIST-1 system, we explore how ultracool dwarfs facilitate the measurement of the spin-orbit angle for Earth-sized planets by creating an effect that can be an order of magnitude more ample than the Doppler reflex motion caused by the planet if the star is undergoing rapid rotation. In TRAPPIST-1's case we expect the Rossiter-McLaughlin semi-amplitudes to be 40–50 m s⁻¹ for the known transiting planets. Accounting for stellar jitter expected for ultracool dwarfs and instrumental noise, and assuming radial velocity precisions both demonstrated and anticipated for upcoming near-infrared spectrographs, we quantify the observational effort required to measure the planets' masses and spin-orbit angles. We conclude that if the planetary system is well-aligned then β can be measured to a precision of $\lesssim 10^\circ$ if the spectrograph is stable at the level of 2 m s⁻¹. We also investigate the measure of $\Delta\beta$, the mutual inclination, when multiple transiting planets are present in the system. Lastly, we note that the rapid rotation rate of many late M-dwarfs will amplify the Rossiter-McLaughlin signal to the point where variations in the chromatic Rossiter-McLaughlin effect from atmospheric absorbers should be detectable.

Key words: planetary systems: atmospheres, planetary systems: detection, planetary systems: terrestrial planets, planetary systems: individual: TRAPPIST-1, stars: late-type, techniques: radial velocities

1 INTRODUCTION

The Rossiter-McLaughlin effect is an anomalous radial velocity signal first observed in eclipsing binary systems and more recently in transiting exoplanetary systems (Rossiter 1924; McLaughlin 1924). As opposing stellar limbs are systematically occulted by a transiting planet, the symmetry of stellar emission from each point on the stellar disc is broken as some starlight is blocked by the planet. If the star has any intrinsic rotation then the transit will cause an excess of particularly Doppler-shifted photons to be observed. This gives rise to the anomalous Rossiter-McLaughlin (RM) signal affecting radial velocity measurements made during transit. The resulting RM waveform is therefore sensitive to the planet's orbital trajectory across the stellar disc and hence to the alignment of the stellar spin axis with the nor-

mal to the planet's orbital plane. The RM effect is therefore suitable to measurement of the so-called sky-projected spin-orbit angle or simply spin-orbit angle as it will be referred to for the remainder of this paper (Ohta et al. 2005; Giménez 2006). Detection of the RM effect and hence the measurement of the spin-orbit angle is useful for probing the orbital history of a planetary system (Fabrycky & Winn 2009; Triaud et al. 2010; Albrecht et al. 2012) as well-aligned planets are predicted from models of terrestrial planet formation and highly misaligned systems may be reconciled with past dynamical events such as planet-planet interactions (Rasio & Ford 1996; Weidenschilling & Marzari 1996) or Kozai migration (Wu & Murray 2003).

Because the RM effect arises from the differential occultation of Doppler-shifted stellar limbs, the semi-amplitude of the RM effect scales with the projected stellar rotation

velocity $v \sin i_s$ ¹ and is also dependent on the transit depth (Gaudi & Winn 2007). In this way, giant planets around rapidly rotating stars become the optimal candidates for observing the RM effect. Following the scaling of the RM semi-amplitude with transit depth and $v \sin i_s$, numerous studies of the RM effect for hot Jupiters have been performed (e.g. Queloz et al. 2000; Triaud et al. 2010; Albrecht et al. 2012; Brown et al. 2012). Furthermore, the RM effect due to small rocky planets is often below the detection threshold of current velocimeters unless the planet’s host star is also small. Fortunately, such planets are common around the M-dwarf class of small stars (Dressing & Charbonneau 2013, 2015; Gaidos et al. 2016) and M-dwarf rotation periods appear to contain a significant population of fast rotators ($P_{\text{rot}} \lesssim 2$ days; Irwin et al. 2011; McQuillan et al. 2013, 2014), especially among the closest M-dwarfs Newton et al. (2016), for which the RM effect of Earth-like planets may be sufficiently large to be detected.

In preparation for the ultracool dwarf transit survey instrument *SPECULOOS* (Gillon et al. 2013a), a pilot survey conducted by the *TRAPPIST* telescope (Gillon et al. 2011) was used to monitor the brightest ultracool dwarfs ($T_{\text{eff}} < 2700$ K; Kirkpatrick et al. 1995) in the Southern Hemisphere, like was done for Luhman-16AB Gillon et al. (2013b). Recently (Gillon et al. 2016, hereafter G16) reported the discovery of a planetary system composed of three Earth-like planets, all transiting a nearby ultracool dwarf now known as TRAPPIST-1 (2MASS J23062928–0502285). This system represents a superlative opportunity to observe the RM effect of rocky planets. The planetary system contains a minimum of three small ($r_p < 1.2 R_{\oplus}$) transiting planets (transit depths $\gtrsim 0.67\%$) with orbital periods of < 20 days, although the orbital period of the outermost planet is not unambiguously detected due to the small number of observed transits coupled with discontinuous observations. This makes the interpretation of the outermost planet indefinite. However, given the planets’ small observed radii it is expected that the planets have bulk rocky compositions (Dressing et al. 2015; Lopez & Fortney 2014) although spectroscopic follow-up observations are likely required to characterize the planet masses thus constraining their bulk densities. The star TRAPPIST-1 is a late M-dwarf (M7.5; Gizis et al. 2000) with spectroscopically measured $v \sin i_s = 6 \pm 2 \text{ km s}^{-1}$ (Reiners & Basri 2010) (see Table 1 for a summary system properties). From this we estimate the RM semi-amplitudes to be $K_{\text{RM}} \sim 40 - 50 \text{ m s}^{-1}$ or an order-of-magnitude greater than the planets’ expected Doppler semi-amplitudes².

In this letter we investigate the radial velocity observations required to study the spin–orbit angles of Earth-like planets around cool stars using the TRAPPIST-1 planetary system as our fiducial test case. In Sect. 2 we explain our methods of constructing synthetic radial velocity timeseries, followed by an explanation in Sect. 3 of our model fitting procedures. Our results are then reported in Sect. 4 followed by a discussion in Sect. 5 and conclusions in Sect. 6.

¹ We reserve the notation i_s for the inclination of the stellar spin axis to the line-of-sight and i_p for planetary orbital inclinations relative to the plane of the sky.

² Sometimes referred to as the ‘orbital’ semi-amplitude in the literature.

2 RADIAL VELOCITY TIMESERIES CONSTRUCTION

In order to investigate the effort required to recover the spin–orbit angles of the two innermost TRAPPIST-1 planets, we perform an extensive Monte-Carlo simulation of the expected radial velocity timeseries under realistic observing conditions, model the RM effect, and quantify the detection significance of the model parameters of interest including the spin–orbit angle. The details of our simulations are discussed below.

2.1 Window Function

The window function defines the epochs at which radial velocity measurements are made. To measure the masses of the two innermost TRAPPIST-1 planets we construct window functions containing N_{obs} measurements made outside of transit so as not to be contaminated by the anomalous RM effect. The full width of the window functions span ~ 6 months assuming that dedicated observations of the star are being executed at most twice per night. The epochs from which we draw from are generated from the TRAPPIST-1 ephemeris with observations obtained at the location of the La Silla Observatory in Chile.

The window functions within transit are sampled separately in order to control the number of observations used to measure the RM effect and constrain β . Due to the short transit widths of the two innermost planets ($\lesssim 42$ minutes) and the typical integration time of 15 minutes plus overhead, in order to obtain well-sampled transit windows requires numerous transits in which at most two radial velocity measurements can be made. This can potentially introduce astrophysical noise in the RM timeseries as levels of stellar jitter may vary between transit events. The effect of the integration time on the amplitude of the RM effect is discussed in Sect. 2.4.

For each unique set of timeseries hyperparameters (i.e. N_{obs} both inside and outside of transit), we generate ten independent window functions to search for planets. In this way, we can marginalize over the hyperparameters when calculating the planet mass and β measurement uncertainties.

2.2 Planetary Signals

Radial velocity (RV) timeseries of the star with planetary companions will contain a number of components which may or may not have an astrophysical origin. The first component arises from the gravitational influence of the three TRAPPIST-1 planets reported in G16. We model these contributions as the superposition of three keplerian orbits with the orbital periods shown in Table 1. Although the orbital period of TRAPPIST-1d is not significantly well-constrained by the current data, we adopt the ‘most-likely’ value from G16 but do not attempt to recover the mass or spin–orbit angle of this planet in our simulations. To compute planetary masses from their observed radii, we assume a bulk Earth-like density. This mass-radius relationship for planets with $r_p \gtrsim 1.6 R_{\oplus}$ is supported by the highest precision measurements of transiting planets (Dressing et al. 2015) and from theoretical planet formation studies of sub-Neptune sized objects (Lopez & Fortney 2014). Our sim-

plified mass-radius relationship results in a conservative estimate of planetary masses compared to that which is obtained by other, empirically derived mass-radius parameterizations (Cloutier et al. *in prep*). The resulting planet masses are $m_p = 1.379, 1.154, 1.573 M_{\oplus}$ for TRAPPIST-1b, c, and d respectively. Following the analysis in G16, each orbit is assumed circular resulting in Doppler semi-amplitudes of $K_{\text{Dop}} = 4.14, 2.96, 2.06 \text{ m s}^{-1}$ for TRAPPIST-1b, c, and d respectively.

One caveat of the keplerian model may arise from the compactness of the planetary system, particularly the two innermost planets, wherein mutual interactions between the planets may not be negligible despite the planets' small semimajor axes and therefore efficient tidal circularization. Any planet-planet interactions may be able to introduce small non-zero eccentricities. However any such eccentricities are expected to be small and we therefore ignore their effects in our analysis. Furthermore, we've declined the use of a fully dynamical model due to the planetary transit light curves not exhibiting any significant transit-timing or transit-duration variations (G16) and thus justifying the adopted keplerian model as a realistic approximation.

Additional planets on wide orbits are posited to exist in this system which would certainly contribute to the observed radial velocity signal. However this prediction is not testable with the currently available data so we limit the number of dynamical components to the number of known planets in the TRAPPIST-1 system. Furthermore, we note that regarding Earth-like planets in other M-dwarfs systems, the average number of small planets per M-dwarf is ~ 2.5 (Dressing & Charbonneau 2015) so the inclusion of 3 planets in our synthetic timeseries are naturally representative of the dynamical contribution from small planets in typical M-dwarf systems.

2.3 Stellar Jitter

Low mass stars undergoing rapid rotation, such as those required to exhibit a detectable RM effect from small planets, are known to often exhibit correspondingly large levels of stellar activity (Mohanty & Basri 2003; Browning et al. 2010; Reiners et al. 2012; West et al. 2015) whose signals will be manifested in the observed radial velocities. G16 used the photometric light curve to measure the stellar rotation period of TRAPPIST-1 to be ~ 1.4 days. The quasi-periodic photometric variability is attributed to the rotation of active regions in the stellar photosphere such as spots and plages which contribute to the radial velocity signal in two distinct ways: i) as the active regions traverse the stellar disc they will disturb its axial symmetry, similar to the RM effect, thus causing a radial velocity variation that scales with the fractional surface coverage by active regions and its first derivative and ii) active regions will suppress the convective blueshift at the photospheric boundary (Aigrain et al. 2012). We find that the former is the dominant source of RV jitter from active regions for rapidly rotating stars such as TRAPPIST-1 and is referred to as the flux effect.

An additional source of RV jitter arises from the Zeeman broadening of spectral features in stars with significant magnetic fields. Reiners et al. (2013) argued that the Zeeman RV jitter is proportional to the square of the magnetic field strength and increases towards longer wavelengths as the

Zeeman displacement itself grows with wavelength. Reiners & Basri (2010) measured the magnetic field strength of TRAPPIST-1 to be 600 Gauss. From this we compute the RV jitter from Zeeman broadening to be a strong contributor to the jitter but still with a smaller amplitude than the flux effect as a result of its relatively weak magnetic field strength.

Both the flux effect and Zeeman broadening dominate the RV jitter budget over the suppression of convective blueshift and each depend on the relative fraction of active region coverage over time. The fractional coverage by active regions is derived from the photometric light curve of TRAPPIST-1 (G16). Using the light curve to derive the total RV jitter, we find that TRAPPIST-1 exhibits a large jitter signal ($\sim 20 \text{ m s}^{-1}$) compared to any gravitationally induced signals resulting from its rapid rotation. The RV jitter model is evaluated in the near-IR at J band ($\lambda \sim 1.2 \mu\text{m}$) throughout this work. The short rotation period of TRAPPIST-1 is typical among the subset of late M-dwarfs which are rapidly rotating. Hence, our fiducial case of TRAPPIST-1 is representative of the population of M-dwarf systems conducive to the detection of the RM effect from an Earth-like planet (see Sect. 5.4).

The large level of RV jitter should be present for TRAPPIST-1 despite the small amplitude of the star's photometric variability and low activity levels (Schmidt et al. 2007; Lee et al. 2010; Reiners & Basri 2010; Gillon et al. 2016). Fortunately, due to the fact that the radial velocity jitter is modulated by active regions³ which evolve in a quasi-periodic manner, we can use the observed photometric variability to model the RV jitter and partially remove it from the observed radial velocities whilst preserving the signal induced by planetary companions which do not affect the star's light curve outside of their transit windows. We note an important assumption made in this critical step: in order to partially mitigate the stellar jitter we must assume that the star's activity properties (e.g. the fractional coverage, spatial distribution, and differential rotation of active regions) do not vary over many rotation cycles. Alternatively, one may obtain contemporaneous photometry and radial velocities to measure the fractional coverage by active regions in real time. Unfortunately this is often not feasible for these types of observations and observers are forced to use additional ancillary timeseries such as line indicators (e.g. $\log R'_{\text{HK}}$) or the bi-sector inverse slope. The accuracy with which the stellar jitter can be removed using photometry is primarily determined by the photometric precision which we adopt from G16. Using the formalism from Aigrain et al. (2012) to model the flux effect and the approximate scaling of the Zeeman broadening from Reiners et al. (2013), we reduce the level of stellar jitter down to an rms of $\sim 4 \text{ m s}^{-1}$ from $\sim 20 \text{ m s}^{-1}$ which is comparable to the noise level of prescribed instrumental/systematic uncertainties (see Sect. 2.5). The use of novel machine learning techniques such as Gaussian process regression to model the stellar jitter may be able improve the residual rms to even

³ We assume that the jitter induced by granulation (i.e. not associated with active regions) can be averaged down via long integration times (Lovis et al. 2005).

lower levels depending on the value of σ_{RV} (Cloutier et al. *in prep*).

TRAPPIST-1, and other cool stars, can potentially exhibit stochastic flares in their light curves on a typical timescale of minutes to hours (Davenport et al. 2014; Gillon et al. 2016). Reiners (2009) argued that these energetic flares are easily distinguishable in spectral orders containing prominent emission lines (e.g. H α , H δ , with optical spectrographs, or with near-IR spectrographs, P γ , P δ in Y-band, and Br γ in K-band; Schmidt et al. 2012) which are excited beyond the stellar quiescent state during flaring events. Following Reiners (2009) we assume that these events can be identified from the sudden presence of the aforementioned emission signatures and the corresponding radial velocity measurements can be excluded when modelling planets.

2.4 Rossiter-McLaughlin Effect

The Rossiter-McLaughlin effect of the two inner-most planets is modelled using the equations from Giménez (2006). The relevant stellar and planetary parameters from Table 1 are used to compute the models. Because transit widths for small planets around M-dwarfs are typically on the order of ~ 30 – 120 minutes, the integration time required to measure the stellar radial velocity (typically 15–20 minutes) occupies a significant fraction of the transit window. To account for this we smooth the RM model over bins with a width equal to the 15 minute integration time. This effect reduces the RM semi-amplitude to below its maximum theoretical value thus making the RM effect more difficult to detect.

Because the structure of the RM effect, and hence K_{RM} , span a range of forms, the maximum value of K_{RM} is realized at $\beta = 0^\circ$ and goes to zero as $|\beta| \rightarrow 90^\circ$. Therefore we separately consider four cases of the planetary spin-orbit angle $\beta = 0^\circ, 30^\circ, 60^\circ, 90^\circ$ where the $\beta = 0^\circ$ corresponds to a perfectly aligned orbit and $\beta = 90^\circ$ corresponds to a planetary orbital plane parallel to the stellar spin axis wherein no RM effect is generated as the planet only occults the region of the stellar disc whose rotation velocity is purely tangential to the line-of-sight. We do not consider retrograde orbits by their waveform symmetry with the spin-orbit angles sampled. Because the empirical distribution of mutual inclinations for small planets around M-dwarfs shows that these systems favour co-planarity (Figueira et al. 2012; Fabrycky et al. 2014), we assign a common value of β to each planet in each simulation.

2.5 Non-Astrophysical Noise

Finally we add an additional noise model which is not astrophysical in nature as it is determined by the experiment’s instrumentation. Explicitly we add a conservative white noise contribution at the level of 6 m s^{-1} akin to the level of RV precision demonstrated by near-IR velocimeters so far. To address cases of the next generation of near-IR velocimeters (e.g. SPIRou; Thibault et al. 2012; Artigau et al. 2014, CARMENES; Quirrenbach et al. 2014, HPP Mahadevan et al. 2012, and IRD spectrograph Tamura et al. 2012) we also consider an improved level of RV precision of 2 m s^{-1} . In addition we add a systematic noise term to account for any non-Gaussian noise and allows us to vary the global

noise properties of the radial velocity timeseries in a simple parametric way.

For reference, examples of our timeseries for TRAPPIST-1b and c are shown in Fig. 1 for the two values of RV precision considered. Each timeseries is phase-folded to the planet’s orbital period and has the keplerian models from the other two planets removed. For clarity, measurements made in-transit are excluded from plots of the full RV timeseries because their values can be an order of magnitude greater than the planet’s Doppler semi-amplitude. The large amplitude RM waveforms are then shown below each full RV timeseries for the $\beta = 0^\circ$ case. In these RM panels, measurements made outside of the transit window are excluded.

3 PLANET MODEL FITTING

As we are interested in the recovery of the RM effect due to the two innermost planets, we must first obtain the best-fit keplerian model to remove from the dataset and search for the RM signature in the residuals. We use the `emcee` (Foreman-Mackey et al. 2013) Markov chain Monte-Carlo ensemble sampler to recover the keplerian model parameter posterior probability density functions (PDF). Because the planetary orbital periods and times of mid-transit are so well constrained by their transit light curves, we take their values to be absolute. Hence we are left with just three free parameters, namely, the RV semi-amplitudes of each of the three planets. This limits the extent of the model parameter posterior probability space and decreases the MCMC’s wall time.

For each synthetic RV timeseries (see Sect. 2) we allocate 100 walkers to explore the model parameter space. Each walker is initialized in a Gaussian ball around the approximate ‘true’ model parameter values. The walkers act as correlated Markov chains, each with a burn-in length defined such that the chains run for ~ 9 – 12 autocorrelation times to ensure that we obtain the equivalent number of independent samples of the target parameter posterior PDFs. Following the burn-in phase, the walkers are extended to another 9–12 autocorrelation times in order to compute the model posterior PDFs and constrain the measurement uncertainty on each parameter. Furthermore, the mean acceptance fraction among the walkers is monitored throughout the MCMC simulations and modifications to the walker initialization, or seldomly to the acceptance fraction scale parameter⁴, are used to constrain the mean acceptance fraction to an ideal range of ~ 20 – 50% .

Given the estimates of TRAPPIST-1 planet masses and their measured orbital periods, we are confident that their RV semi-amplitudes are $< 10 \text{ m s}^{-1}$. From this we adopt a common, uniform prior on each planet’s semi-amplitude; $K \in \mathcal{U}(0, 10) \text{ m s}^{-1}$. Furthermore we adopt the Gaussian likelihood function proposed by Gregory (2010) in our MCMC.

Following the recovery of the maximum *a posteriori*

⁴ The scale parameter can be used to tune the probability that a proposed step in each walker’s chain is accepted or rejected. See Sect. 4 of Foreman-Mackey et al. (2013)

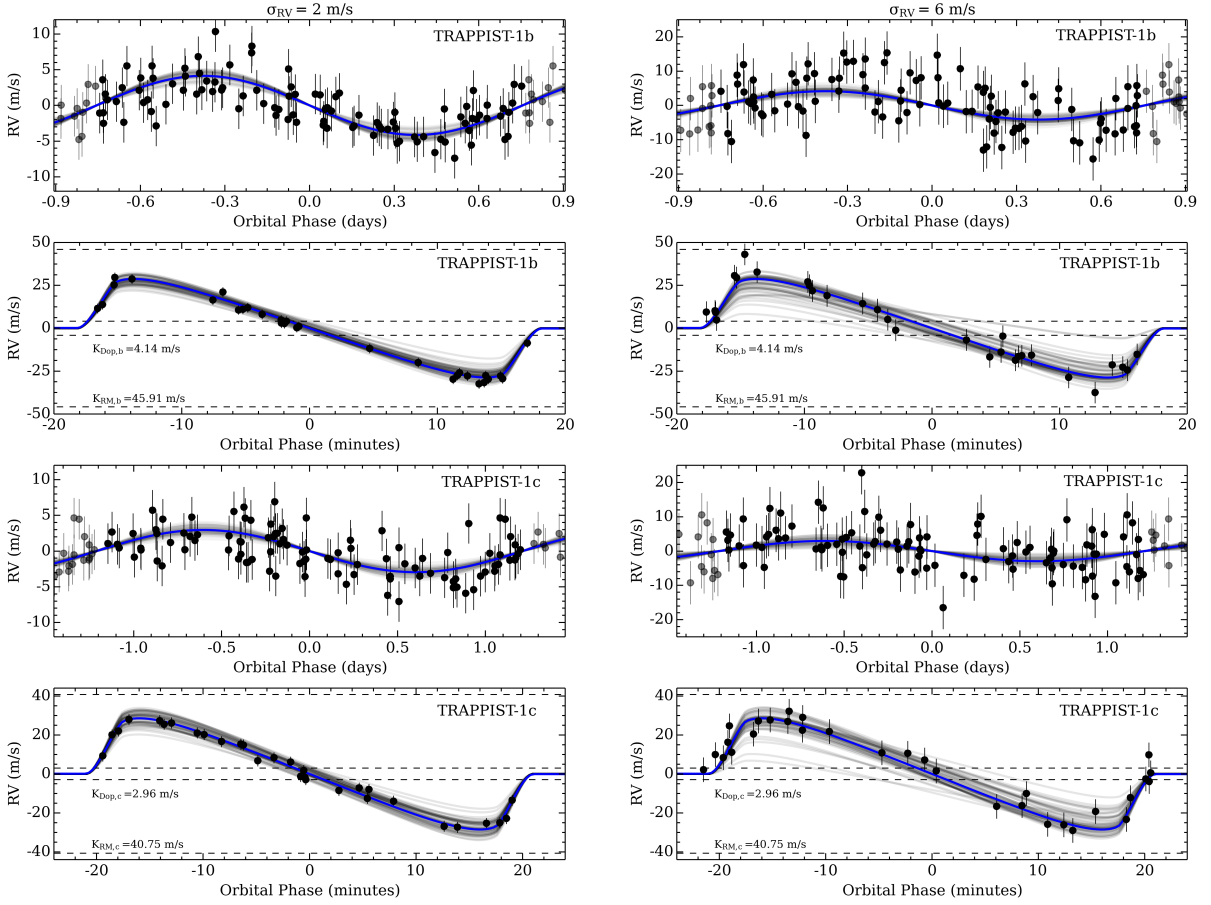


Figure 1. Sample phase-folded, simulated radial velocity timeseries for TRAPPIST-1b and c with $\sigma_{RV} = 2 \text{ m s}^{-1}$ (left panels) and $\sigma_{RV} = 6 \text{ m s}^{-1}$ (right panels). Directly beneath each full RV timeseries is a close-up view of the transit window revealing the Rossiter-McLaughlin effect. In all panels the *true* model from which the data are derived is shown in *blue*. Models computed from random draws from the model parameter posterior distributions are shown in *translucent grey*. The *horizontal dashed lines* in the RM panels illustrate the Doppler semi-amplitude of the corresponding planet and the semi-amplitude of the Rossiter-McLaughlin effect in the absence of smoothing the observations over the integration time. For clarity, the full RV panels do not contain any measurements made in-transit while the RM panels do not contain measurements made outside of transit.

(MAP) RV semi-amplitudes, we couple those parameter values to the planetary orbital parameters and compute the MAP keplerian models. These models are removed from the timeseries and we proceed to search for the RM waveform in the residuals. Specifically we focus on the time interval spanning one transit duration prior to transit ingress and following transit egress (≈ 100 minutes and ≈ 125 minutes for TRAPPIST-1b and c respectively).

Fixing most planetary and stellar model parameters in the Giménez (2006) models of the RM effect, we set the free parameters in the MCMC to $\sqrt{v \sin i_s} \cos \beta$ and $\sqrt{v \sin i_s} \sin \beta$. This prescription follows from Triaud et al. (2011) for the purpose of reducing correlations among the free model parameters. The MCMC is then run identically as above to obtain independent measurements of $v \sin i_s$ and the spin-orbit angle β . The limits on our adopted uniform prior on $v \sin i_s$ are set by the fact that $v \sin i_s$ must be $> 0 \text{ km s}^{-1}$ for non-zero inclination⁵ and the 3σ uncer-

tainty on $v \sin i_s$ from spectroscopic measurements. Hence, $v \sin i_s \in \mathcal{U}(0, 12) \text{ km s}^{-1}$. As we have effectively no *a priori* knowledge of the planetary spin-angles in the system⁶, we must consider the full range of possible spin-orbit angles: $\beta \in \mathcal{U}(-\pi, \pi)$.

For some test cases with various input spin-orbit angles, we compared the results of our MCMC analysis of the RM effect when using the aforementioned uniform prior to the use of the Jeffreys non-informative prior. We found that the resulting MAP $v \sin i_s$ and β values and their uncertainties were effectively unchanged by our choice of prior.

⁶ Aside from the empirical evidence that small planets rarely undergo high eccentricity migration (e.g. Figueira et al. 2012; Fabrycky et al. 2014) therefore favouring well-aligned orbits; $\beta \sim 0^\circ$.

⁵ It is expected that $i_s \neq 0^\circ$ given that periodic modulations are observed in the TRAPPIST-1 light curve (G16).

4 RESULTS

4.1 Recovery of Planet Masses

Before we can investigate the measurement precision of the spin-orbit angle β , we require an orbital solution for the system. The best-fit orbital solution from MCMC will be removed from the radial velocity timeseries which allows one to search the residuals for the anomalous RM effect within each of the two inner planets' known transit windows. Any discrepancy between the best-fit orbital solution and the 'true' planetary orbits will introduce an additional source of error into the residual timeseries and affect the accuracy with which the spin-orbit angle can be measured.

A product of the first set of MCMC simulations from Sect. 3 is the posterior PDFs of the planet keplerian semi-amplitude solutions K_i for $i = \text{b,c,d}$. We take the parameter uncertainties to be 16th and 84th percentiles (1σ if the PDF is Gaussian) of the posterior PDF and the best-fit value to be the MAP value. Knowledge of the K_i uncertainties are crucial as they will ultimately affect the precision of our best-fit orbital model and therefore our ability to accurately measure β . Using the MCMC recovered values of K_i , the orbital period, orbital inclination, and stellar mass from Table 1, we use the standard method of error propagation to compute the MAP planet mass m_p and its associated uncertainty σ_{m_p} from each synthetic RV timeseries. We then define the mass detection significance as m_p/σ_{m_p} . Fig. 2 shows the median mass detection significance for each of the two inner planets as a function of the number of RV measurements used to fit the model. The uncertainty in each N_{obs} bin is calculated from the median absolute deviation of the mass detection significances within that bin.

As expected, the mass detection significance increases monotonically with N_{obs} and appears to asymptotically approach a maximum mass detection significance which requires additional simulations with $N_{\text{obs}} > 200$ to measure. Furthermore, the mass detection significance of TRAPPIST-1b is always greater than for TRAPPIST-1c due to its larger Doppler semi-amplitude.

Considering the σ_{RV} cases separately, unsurprisingly we see that it has a significant effect on the mass detection significance for a given number of RV measurements. In particular, for $\sigma_{\text{RV}} = 2 \text{ m s}^{-1}$ a 3σ mass detection for TRAPPIST-1b or c is achieved with ~ 20 and 40 measurements respectively and for TRAPPIST-1b increases to a $\geq 5\sigma$ detection with $N_{\text{obs}} \gtrsim 60$. TRAPPIST-1c requires $N_{\text{obs}} \sim 120$ in order to achieve a 5σ . These results for $\sigma_{\text{RV}} = 2 \text{ m s}^{-1}$ are broadly consistent with the mass detection significance of GJ 1132b (Berta-Thompson et al. 2015), a rocky planet transiting a nearby mid-M-dwarf (Cloutier et al. *in prep*). If the RV measurement uncertainty is degraded to $\sigma_{\text{RV}} = 6 \text{ m s}^{-1}$, the mass detection significance is reduced. Namely, a 3σ mass detection of TRAPPIST-1b (c) requires $N_{\text{obs}} \sim 90$ (~ 180). Furthermore, even with 200 measurements, the mass detection significance is always $< 5\sigma$ for either planet. Clearly, a RV uncertainty of 6 m s^{-1} compared to 2 m s^{-1} significantly deters one's ability to detect small transiting planet masses in RV with a modest number of RV measurements ($N_{\text{obs}} \lesssim 100$).

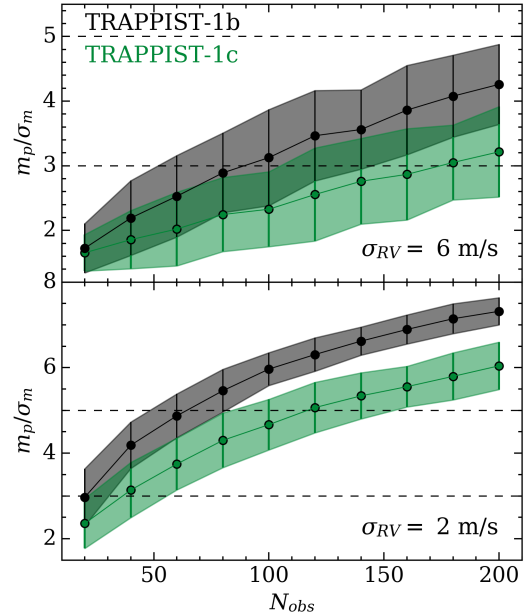


Figure 2. The mass detection significance, m_p/σ_{m_p} , as a function of the number of the radial velocity measurements used to fit the Doppler semi-amplitudes, for two values of the fixed radial velocity uncertainty; $\sigma_{\text{RV}} = 2 \text{ m s}^{-1}$ (top) and $\sigma_{\text{RV}} = 6 \text{ m s}^{-1}$ (bottom). The shaded regions highlight the approximate 1σ confidence intervals for each planet. Horizontal dashed lines are used to indicate a 3 and 5σ mass detection in each panel.

4.2 Detecting the RM effect and Spin-Orbit Angle Measurements

Using the keplerian model solutions described in Sect. 4.1, we are in a position to model the RM effect in the RV residuals. Given the unique opportunity to detect the RM effect of Earth-like planets around small stars, we are interested in quantifying the spin-orbit angle measurement precision achievable. Fig. 3 shows the average measurement uncertainty of the spin-orbit angle σ_β between the two innermost planets for $\sigma_{\text{RV}} = 2$ and 6 m s^{-1} . Only the RV measurements made within the planet's transit window are used to fit the RM waveform and measure β .

As was seen with the planet mass measurements in Fig. 2, the spin-orbit angle measurement uncertainty in Fig. 3 decreases monotonically with N_{obs} . At a given value of N_{obs} , the absolute value of σ_β decreases for increasing β from 0° to 90° . This is due to the general trend of decreasing K_{RM} as $|\beta| \rightarrow 90^\circ$ for the impact parameters of the TRAPPIST-1 planets since the dispersion of the RM waveform about the radial velocity zeropoint is minimized for $\beta = 90^\circ$ implying that as the structure in the waveform increases, more values of β become consistent with the data at a given σ_{RV} causing the measurement uncertainty to grow.

Although we do not yet have a statistically significant sample of spin-orbit angles of Earth-like planets, their observed low mutual inclinations in multi-planet systems suggests that their orbital alignments will be consistent with $\beta = 0^\circ$ as a result of their cold dynamical histories (Figueira et al. 2012; Fabrycky et al. 2014). Focusing on this well-aligned case, it is apparent that σ_β will be large ($\sigma_\beta > 10^\circ$)

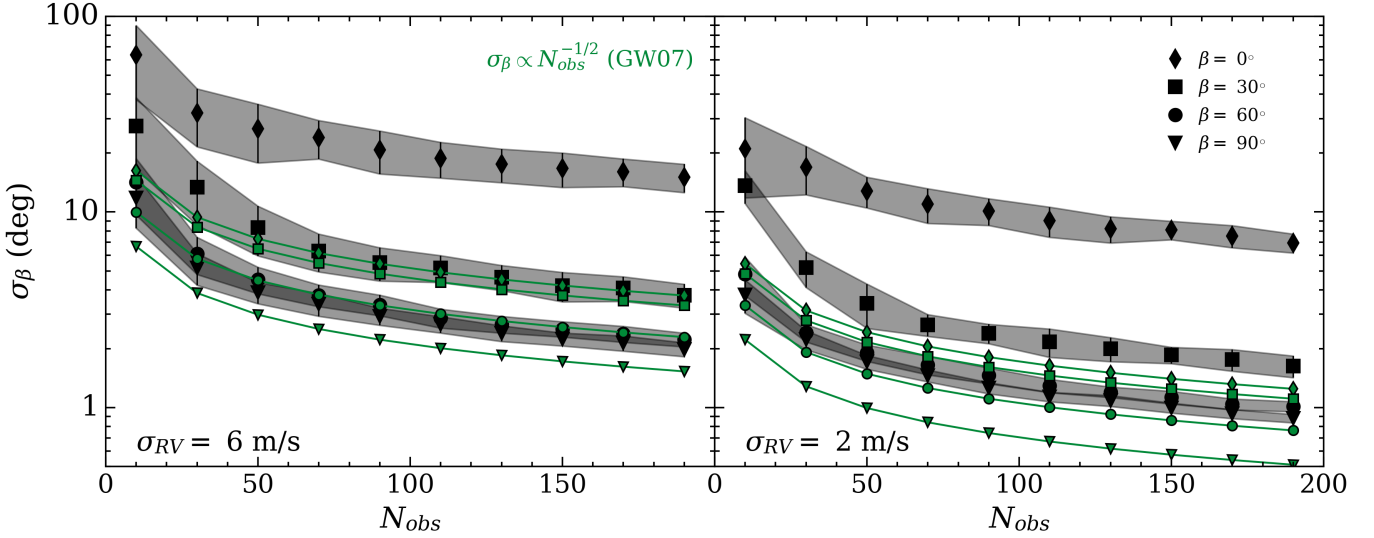


Figure 3. The average measurement uncertainty of the spin–orbit angle for TRAPPIST-1b and c from the measurement of the Rossiter–McLaughlin waveform as a function of the number of radial velocity measurements made in-transit. Values of $\beta = 0^\circ, 30^\circ, 60^\circ, 90^\circ$ are considered for both cases of the radial velocity measurement uncertainties ($\sigma_{RV} = 6 \text{ m s}^{-1}$; *left* and $\sigma_{RV} = 2 \text{ m s}^{-1}$; *right*). The shaded regions approximately depict the 1σ confidence intervals from the dispersion in σ_β after multiple Monte-Carlo realizations. The *green curves* represent the predicted measurement uncertainty from *GW07*.

even up to $N_{\text{obs}} = 190$ if σ_{RV} is large (6 m s^{-1}).⁷ In order for σ_β to be $< 20^\circ$, N_{obs} must be $\gtrsim 110$. This improves dramatically if σ_{RV} is reduced to 2 m s^{-1} with $\sigma_\beta < 20^\circ$ when $N_{\text{obs}} \gtrsim 10$ and $\sigma_\beta \sim 7^\circ$ at $N_{\text{obs}} = 190$. Furthermore, each of the $\beta = 0^\circ$ curves shown in Fig. 3 appear to approach a minimum value of σ_β close to the aforementioned values implying that additional RV measurements do not drastically improve your β measurement precision. In practice, $\sigma_\beta \sim 7^\circ$ ($\sigma_\beta \sim 16^\circ$) for $\sigma_{RV} = 2 \text{ m s}^{-1}$ ($\sigma_{RV} = 6 \text{ m s}^{-1}$) provides the most stringent precision with which we can measure β unless many hundreds more observations can be obtained or the RV rms can be decreased either by more accurate modelling of the stellar jitter and/or by improving the instrument’s RV stability (*Cloutier et al. in prep*).

Complimentary to our empirical estimate of the spin–orbit angle measurement uncertainty, (*Gaudi & Winn 2007*, hereafter *GW07*) presented an analytical calculation of σ_β which differs from our results but are fairly consistent with certain observational results of hot Jupiters (e.g. *Triaud et al. 2010*). We attribute the discrepancies between the two studies to differences in the noise properties of the observed timeseries. Unlike in *GW07*, our RV timeseries include significant non-white noise contributions from stellar jitter (see Sect. 2.3) that are partially removed, leaving behind RV residuals that differ substantially from white. This is not the case in the test cases presented in *GW07* or in the observational studies which roughly agree with the *GW07* estimation of $\sigma_\beta(N_{\text{obs}})$. This is because those systems containing hot Jupiters exhibit planetary signals that are large

compared to the stellar jitter unlike the case of Earth-like planets around rapidly rotating, small stars.

The analytic expression of *GW07* ($\sigma_\beta \propto N_{\text{obs}}^{-1/2}$; see their Eq. 16) is over-plotted in Fig. 3. This expression underestimates the spin–orbit angle measurement uncertainty for each value of β as a result of the dominant noise properties being non-white. In addition to differences in the noise properties, discrepancies are derived from the differences in their respective methodologies. The expression in *GW07* is derived from the Fisher information in those systems and an analytical prescription of the RM waveform under the assumption of large N_{obs} and measurements which are uniformly sampled in time. Conversely, our method of deriving σ_β is intended to mimic that of a realistic observing procedure wherein a sampling method (e.g. MCMC) is used to compute the RM model parameter posterior probability distributions from which measurement uncertainties are derived. In this way our methodology is independent of the approximations made when deriving an analytical approximation and is representative of how model parameter uncertainties are derived in practise. Indeed this is the procedure used in a number of observational studies of the RM effect (e.g. *Queloz et al. 2010*; *Triaud et al. 2010*).

5 DISCUSSION

5.1 Constraints on Planetary System Alignment

If the RM effect is detected for each of TRAPPIST-1b and c, then we can compute the spin–orbit angle difference $\Delta\beta = \beta_b - \beta_c$ and its corresponding precision. This quantity is useful for determining whether or not the planetary system is mutually aligned. For instance, a value of

⁷ We note that obtaining such a large number of in-transit measurements, with at most two measurements per observed transit, is difficult in practise as the timescale for doing so likely exceeds that of a single observing season.

$\Delta\beta \neq 0$ provides evidence for independent dynamical histories among the two planets. Recall that during the construction of the RM timeseries, $\Delta\beta = 0^\circ$ was imposed in all cases. From measurements of β_b and β_c and their uncertainties (see Fig. 3) the uncertainty on $\Delta\beta$ can easily be computed via the product of σ_β with $\sqrt{2}$ from the propagation of errors as the uncertainty in β_b and β_c should be equal when $\Delta\beta = 0^\circ$.

To summarize the precision with which we can measure $\Delta\beta$, we focus on the case with $\beta = 0^\circ$, the expected mean result for small planets around ultracool dwarfs. When $\sigma_{RV} = 6 \text{ m s}^{-1}$, $\sigma_{\Delta\beta}$ decreases from $\sim 90^\circ$ for $N_{\text{obs}} = 10$ down to $\sim 21^\circ$ for $N_{\text{obs}} = 190$. Comparatively, when $\sigma_{RV} = 2 \text{ m s}^{-1}$, $\sigma_{\Delta\beta}$ decreases from $\sim 30^\circ$ for $N_{\text{obs}} = 10$ down to $\sim 10^\circ$ for $N_{\text{obs}} = 190$. Of course these values will be smaller for larger values of β but we leave interested readers to estimate $\sigma_{\Delta\beta}$ for themselves using the σ_β curves shown in Fig. 3. For example, for a ‘reasonable’ value of $N_{\text{obs}} = 50$ and $\sigma_{RV} = 2 \text{ m s}^{-1}$, we can measure the misalignment of the planetary orbital planes to $\pm 17^\circ$. This becomes $\pm 40^\circ$ if $\sigma_{RV} = 6 \text{ m s}^{-1}$.

5.2 Atmospheric Studies

The presence of various absorbing species within the atmospheres of exoplanets can be measured using transmission spectroscopy as a variation in the apparent size of the planet with wavelength (Seager & Sasselov 2000). Snellen (2004) and Di Gloria et al. (2015) managed to detect the chromatic RM effect in the atmospheres of the hot Jupiters HD 209458b and HD 189733b respectively. Although de Wit et al. (2016) recently demonstrated that neither TRAPPIST-1b nor c possess a hydrogen/helium dominated atmosphere, recent theoretical studies (e.g. Owen & Mohanty 2016) have shown that such an atmospheric composition still remains a possibility for planets similar to those orbiting TRAPPIST-1 and are expected to be detected with upcoming instrumentation (e.g. SPECULOOS; Gillon et al. 2013a).

For the sake of argument if we adopt TRAPPIST-1b as a fiducial case but include a primarily hydrogen/helium atmospheric composition ($\mu = 2.5$) then one would expect a large pressure scale-height of $\sim 110 \text{ km}$ with an assumed Bond albedo of 0.3 ($T_{\text{eff}} = 365 \text{ K}$). In the absence of clouds, spectral features from near-IR absorbing species (e.g. H_2O and CH_4) mixed into the primarily H/He atmosphere can reach 6-10 scale heights (Miller-Ricci et al. 2009; de Wit & Seager 2013). Taking this lower factor applicable to the Earth (Kaltenegger & Traub 2009), the expected variations in the apparent size of the planet will be of order 1500 ppm in spectral orders containing features from the absorbing species. This increase in opacity translates into a variation in the RM effect semi-amplitude of $\Delta K_{\text{RM}} \sim 9 \text{ m s}^{-1}$. Here $v \sin i_s$ amplifies the atmospheric signal.

For a ‘white-light’ RM semi-amplitude of 45.9 m s^{-1} , an increase of 9 m s^{-1} is a significant increase. From our simulations we found that so long as the RM waveform is well-sampled around its peak velocity, the uncertainty in the projected stellar rotation velocity is always $\lesssim 5 \text{ km s}^{-1}$. This implies that the planetary atmosphere may be measurable with the RM effect at multiple wavelengths and is certainly detectable if indeed the planet’s atmospheric mean molecular weight is dominated by hydrogen and helium and

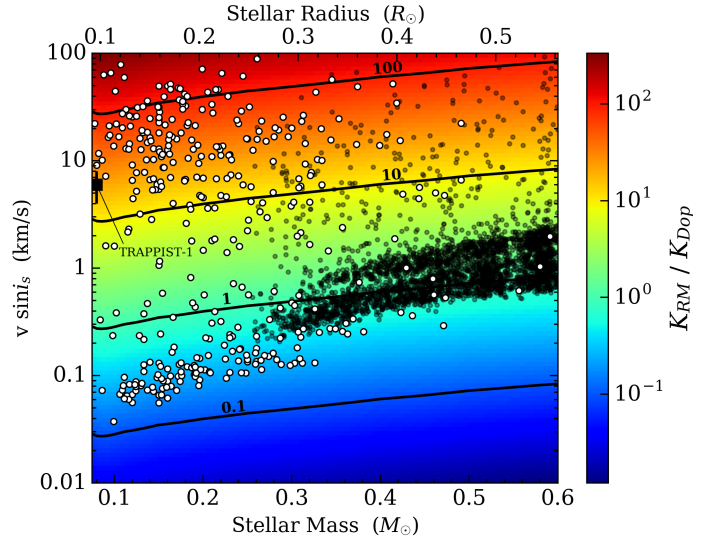


Figure 4. The ratio of the Rossiter-McLaughlin semi-amplitude to the Doppler semi-amplitude for an Earth-sized planet at the inner edge of the habitable zone. White and black symbols depict stellar rotation periods measured with MEarth (Irwin et al. 2011; Newton et al. 2016) and Kepler (McQuillan et al. 2014) respectively. TRAPPIST-1 is depicted as the black square according to its mass. Over the range of observed M-dwarf rotation velocities, the semi-amplitude of the RM effect can be over two orders-of-magnitude less than or greater than the Doppler semi-amplitude of a typical rocky planet in the habitable zone.

the signal-to-noise within the reduced wavelength bins can remain sufficiently high.

5.3 The Rossiter-McLaughlin Effect Around Late-type Stars

The RM effect and hence spin-orbit angles of Earth-like planets has not been well-studied compared to the giant planets. This comes as a result of their often small transit depths and low RM semi-amplitudes. But given the large frequency of small planets around late-type stars and the large subset of stars which are rapidly rotating, there exists many targets for which the RM semi-amplitude of an Earth-like planet may be large compared to the planet’s Doppler semi-amplitude and potentially two orders of magnitude greater. This is evidenced in Fig. 4 which depicts the $K_{\text{RM}}/K_{\text{Dop}}$ ratio as a function of stellar mass and projected stellar rotation velocity for an Earth-sized planet at the inner edge of the habitable zone; one of the most common types of planet around M-dwarfs (Dressing & Charbonneau 2015). The inner edge of the habitable zone is computed at each grid point from the Kopparapu et al. (2013) prescription and the stellar effective temperature derived from the stellar mass at 5 Gyrs assuming solar metallicity (Baraffe et al. 1998), applicable down to $0.075 M_\odot$. The M-dwarf rotation period distribution, converted to $v \sin i_s$ assuming $i_s = 90^\circ$ and deriving the stellar radius from the stellar mass, is over-plotted and shows that a large population of M-dwarfs exists for which $K_{\text{RM}}/K_{\text{Dop}} \gg 1$ and are therefore prime targets for the RM characterization of an Earth-like planet.

5.4 How typical is the TRAPPIST-1 system?

It attempting to characterize the effort required to recover the RM effect due to Earth-like planets around the coolest stars, we have focused our attention on a particular system, namely TRAPPIST-1. Justification of this approximation should be emphasized. Firstly, the consideration of a single system greatly simplifies the computational cost of our study because the parameter space is substantially reduced. Furthermore, we argue that TRAPPIST-1 is a star that is well representative of the ultracool stellar population of interest for the detection of the RM effect from Earth-like planets. Notably, TRAPPIST-1 exhibits a rotation period of 1.4 days from its photometric variability. Irwin et al. (2011) and Newton et al. (2016) showed empirically that this is a typical value among late M-dwarfs over a wide range of ages as these stars can maintain short rotation periods well into their lifetimes (West et al. 2015).

In the limit of small transit depths, such as those typical of small planets around M-dwarfs, K_{RM} approximately scales linearly with transit depth (Gaudi & Winn 2007) such that $K_{\text{RM}} \propto R_s^{-2}$. Because of this, detection of the RM effect favours small stars such as TRAPPIST-1 with $R_s = 0.117 R_{\odot}$. However we argue below that the size of TRAPPIST-1 is representative of the population of stars close to the stellar/substellar boundary ($0.075 \lesssim M_s \lesssim 0.1$).

Because the MS lifetime of stars close to the stellar/substellar boundary exceeds the Hubble time, the typical radius of such stars can be estimated from the stellar IMF in that mass regime (Padoan & Nordlund 2002) coupled with stellar evolutionary tracks applicable to low-mass stars to compute the corresponding stellar radii (Baraffe et al. 1998). The analytical Padoan & Nordlund (2002) IMF increases over this range of stellar masses before peaking around $0.2 M_{\odot}$. Therefore the most common ultracool dwarf is approximately $0.1 M_{\odot}$ which has a model radius of $\sim 0.122 \pm 0.01 R_{\odot}$ by considering the effect of changing metallicity and relative He abundances. This value is consistent with the reported radius of TRAPPIST-1 ($0.117 R_{\odot}$). Therefore, the radius of TRAPPIST-1 is characteristic of the joint population of very low mass stars and brown dwarfs.

The planetary parameters of the TRAPPIST-1 planets are also typical of the population of small planets around late K to early M-dwarfs which we assume extrapolates down towards ultracool dwarfs given the lack observational constraints on the planet occurrence rate around ultracool dwarfs; a population which will be probed by the next generation of high precision near-IR spectrographs (i.e. *SPIRou*; Thibault et al. 2012; Artigau et al. 2014). This extrapolation may be reasonable given the high number of small planets predicted to form around these cool stars via core-accretion (Payne & Lodato 2007).

5.5 Application to Other Systems

The detection of the RM effect for Earth-like planets will be facilitated by the detection of such planets around the smallest stars including late M and brown dwarfs. The detection of the TRAPPIST-1 multi-planetary system in the TRAPPIST telescope science verification runs with just 50 targets, suggests that small planets are common around the smallest stars. This region of the stellar parameter space

has been largely unexplored at present but will be investigated in the near future with dedicated transit (e.g. *SPECU-LOOS*; Gillon et al. 2013a) and radial velocity surveys in the near-IR (e.g. *SPIRou*; Thibault et al. 2012; Artigau et al. 2014, *CARMENES*; Quirrenbach et al. 2014, *HPF* Mahadevan et al. 2012, and *IRD* spectrograph Tamura et al. 2012). The detection significance curves presented in Figs. 2 and 3 will help to inform the search for the RM effect from Earth-like planets around rapidly rotating small stars which will ultimately result in the direct measurement of the distribution of small planet spin-orbit angles; a quantity which is useful for probing the formation pathways of Earth-like planets around small stars.

6 SUMMARY & CONCLUSION

In this study we have shown that the Rossiter-McLaughlin effect due to Earth-like planets is measurable around the class of ultracool dwarfs which includes late M to brown dwarfs. Such measurements are facilitated by the small stellar radii and high fraction of stars undergoing rapid rotation. Taking the TRAPPIST-1 multi-planetary system as a fiducial test case, we compute the detection significance of planetary masses and projected spin-orbit angles, via the Rossiter-McLaughlin effect, by constructing synthetic radial velocity timeseries and using Monte-Carlo simulations to measure the planet parameters of interest and their uncertainties. The main results are summarized as follows:

- Adopting a radial velocity stability of $\sigma_{\text{RV}} = 6 \text{ m s}^{-1}$, a value representative of currently operating near-IR velocimeters, the planet masses of TRAPPIST-1b and c can be detected at the 3σ level with ~ 90 and 180 measurements respectively.
- Decreasing the radial velocity stability to a more sought after level of $\sigma_{\text{RV}} = 2 \text{ m s}^{-1}$, 3σ detections of the planet masses can be obtained with just ~ 20 and 40 measurements respectively.
- Considering the probable cold dynamical histories of small planets around small stars, a projected spin-orbit angle measurement precision of $\sigma_{\beta} < 20^{\circ}$ requires $N_{\text{obs}} \gtrsim 110$ if $\sigma_{\text{RV}} = 6 \text{ m s}^{-1}$.
- If $\sigma_{\text{RV}} = 2 \text{ m s}^{-1}$, this is greatly reduced to just $N_{\text{obs}} \sim 10$ and begins to asymptotically approach a minimum value of $\sigma_{\beta} \sim 7^{\circ}$.
- The significant non-white noise in radial velocity timeseries containing small planets around small, rapidly rotating stars (i.e. significant stellar jitter) causes σ_{β} to be underestimated by analytical approximations derived in the limit of white noise domination (e.g. Gaudi & Winn 2007).
- The resulting uncertainties imply that we cannot measure the difference in projected planetary spin-orbit angles between planets to better than $\sim 10^{\circ}$ when $\beta = 0^{\circ}$.
- The sub-population of rapidly rotating M-dwarfs provides a set of targets for which $K_{\text{RM}} \gg K_{\text{Dop}}$ and represents the optimal targets for the direct measurement of the projected spin-orbit angle distribution for Earth-like planets.
- Variations in the planetary radius due to the presence of various volatiles is shown to result in a change in the TRAPPIST-1b transit depth of ~ 1500 ppm for a H/He dominated atmosphere. This corresponds to a mea-

surable change in the Rossiter-McLaughlin semi-amplitude of $\Delta K_{\text{RM}} \sim 9 \text{ m s}^{-1}$.

Ultimately we are interested in the effort required to measure the projected spin-orbit angle of Earth-like planets via the detection of their Rossiter-McLaughlin effects. The TRAPPIST-1 planetary system represents a superlative target for such observations given the small size of the star and its rapid rotation velocity. Up-coming high precision, near-IR velocimeters will provide the best possible tools for making such measurements which will benefit greatly from achieving the smallest possible radial velocity stability. In the coming years, uncovering the planet population around the coolest stars and detecting their projected spin-orbit angles will be able to shed light on their formation mechanisms and dynamical histories.

ACKNOWLEDGEMENTS

We gratefully acknowledge the *TRAPPIST* team, in particular Michaël Gillon, and thank them for use of the TRAPPIST-1 planetary system parameters. We also thank Scott Gaudi and Joshua Winn for their useful discussions and the anonymous referee for their suggestions which we believe greatly improved the manuscript. RC also thanks the Canadian Institute for Theoretical Astrophysics for use of the Sunnyvale computing cluster throughout this work. RC is supported in part by a Centre for Planetary Sciences Graduate Fellowship.

REFERENCES

- Aigrain S., Pont F., Zucker S., 2012, *MNRAS*, **419**, 3147
- Albrecht S., et al., 2012, *ApJ*, **757**, 18
- Artigau É., et al., 2014, in Society of Photo-Optical Instrumentation Engineers (SPIE) Conference Series. p. 15 ([arXiv:1406.6992](https://arxiv.org/abs/1406.6992)), doi:10.1117/12.2055663
- Baraffe I., Chabrier G., Allard F., Hauschildt P. H., 1998, *A&A*, **337**, 403
- Berta-Thompson Z. K., et al., 2015, *Nature*, **527**, 204
- Brown D. J. A., et al., 2012, *MNRAS*, **423**, 1503
- Browning M. K., Basri G., Marcy G. W., West A. A., Zhang J., 2010, *AJ*, **139**, 504
- Claret A., Bloemen S., 2011, *A&A*, **529**, A75
- Cloutier R., Doyon R., Menou K., Dumusque X., Delfosse X., Artigau É., 2016, *ApJin* prep.
- Davenport J. R. A., et al., 2014, *ApJ*, **797**, 122
- Di Gloria E., Snellen I. A. G., Albrecht S., 2015, *A&A*, **580**, A84
- Dressing C. D., Charbonneau D., 2013, *ApJ*, **767**, 95
- Dressing C. D., Charbonneau D., 2015, *ApJ*, **807**, 45
- Dressing C. D., et al., 2015, *ApJ*, **800**, 135
- Eastman J., Gaudi B. S., Agol E., 2013, *PASP*, **125**, 83
- Fabrycky D. C., Winn J. N., 2009, *ApJ*, **696**, 1230
- Fabrycky D. C., et al., 2014, *ApJ*, **790**, 146
- Figueira P., et al., 2012, *A&A*, **541**, A139
- Foreman-Mackey D., Hogg D. W., Lang D., Goodman J., 2013, *PASP*, **125**, 306
- Gaidos E., Mann A. W., Kraus A. L., Ireland M., 2016, *MNRAS*, **457**, 2877
- Gaudi B. S., Winn J. N., 2007, *ApJ*, **655**, 550
- Gillon M., Jehin E., Magain P., Chantry V., Hutsemékers D., Manfroid J., Queloz D., Udry S., 2011, in European Physical Journal Web of Conferences. p. 06002 ([arXiv:1101.5807](https://arxiv.org/abs/1101.5807)), doi:10.1051/epjconf/20101106002
- Gillon M., Jehin E., Delrez L., Magain P., Opitom C., Sohy S., 2013a, in Protostars and Planets VI Posters.
- Gillon M., Triaud A. H. M. J., Jehin E., Delrez L., Opitom C., Magain P., Lendl M., Queloz D., 2013b, *A&A*, **555**, L5
- Gillon M., et al., 2016, *Nature*, **533**, 221
- Giménez A., 2006, *ApJ*, **650**, 408
- Gizis J. E., Monet D. G., Reid I. N., Kirkpatrick J. D., Liebert J., Williams R. J., 2000, *AJ*, **120**, 1085
- Gregory P., 2010, Bayesian Logical Data Analysis for the Physical Sciences
- Irwin J., Berta Z. K., Burke C. J., Charbonneau D., Nutzman P., West A. A., Falco E. E., 2011, *ApJ*, **727**, 56
- Kaltenegger L., Traub W. A., 2009, *ApJ*, **698**, 519
- Kirkpatrick J. D., Henry T. J., Simons D. A., 1995, *AJ*, **109**, 797
- Kopparapu R. K., et al., 2013, *ApJ*, **765**, 131
- Lee K.-G., Berger E., Knapp G. R., 2010, *ApJ*, **708**, 1482
- Lopez E. D., Fortney J. J., 2014, *ApJ*, **792**, 1
- Lovis C., et al., 2005, *A&A*, **437**, 1121
- Mahadevan S., et al., 2012, in Ground-based and Airborne Instrumentation for Astronomy IV. p. 84461S ([arXiv:1209.1686](https://arxiv.org/abs/1209.1686)), doi:10.1117/12.926102
- McLaughlin D. B., 1924, *ApJ*, **60**, 22
- McQuillan A., Aigrain S., Mazeh T., 2013, *MNRAS*, **432**, 1203
- McQuillan A., Mazeh T., Aigrain S., 2014, *ApJS*, **211**, 24
- Miller-Ricci E., Seager S., Sasselov D., 2009, *ApJ*, **690**, 1056
- Mohanty S., Basri G., 2003, *ApJ*, **583**, 451
- Newton E. R., Irwin J., Charbonneau D., Berta-Thompson Z. K., Dittmann J. A., West A. A., 2016, *ApJ*, **821**, 93
- Ohta Y., Taruya A., Suto Y., 2005, *ApJ*, **622**, 1118
- Owen J. E., Mohanty S., 2016, *MNRAS*, **459**, 4088
- Padoan P., Nordlund Å., 2002, *ApJ*, **576**, 870
- Payne M. J., Lodato G., 2007, *MNRAS*, **381**, 1597
- Queloz D., Eggenberger A., Mayor M., Perrier C., Beuzit J. L., Naef D., Sivan J. P., Udry S., 2000, *A&A*, **359**, L13
- Queloz D., et al., 2010, *A&A*, **517**, L1
- Quirrenbach A., et al., 2014, in Ground-based and Airborne Instrumentation for Astronomy V. p. 91471F, doi:10.1117/12.2056453
- Rasio F. A., Ford E. B., 1996, *Science*, **274**, 954
- Reiners A., 2009, *A&A*, **498**, 853
- Reiners A., Basri G., 2010, *ApJ*, **710**, 924
- Reiners A., Joshi N., Goldman B., 2012, *AJ*, **143**, 93
- Reiners A., Shulyak D., Anglada-Escudé G., Jeffers S. V., Morin J., Zechmeister M., Kochukhov O., Piskunov N., 2013, *A&A*, **552**, A103
- Rossiter R. A., 1924, *ApJ*, **60**, 15
- Schmidt S. J., Cruz K. L., Bongiorno B. J., Liebert J., Reid I. N., 2007, *AJ*, **133**, 2258
- Schmidt S. J., Kowalski A. F., Hawley S. L., Hilton E. J., Wisniewski J. P., Tofflemire B. M., 2012, *ApJ*, **745**, 14
- Seager S., Sasselov D. D., 2000, *ApJ*, **537**, 916
- Snellen I. A. G., 2004, *MNRAS*, **353**, L1
- Tamura M., et al., 2012, in Ground-based and Airborne Instrumentation for Astronomy IV. p. 84461T, doi:10.1117/12.925885
- Thibault S., et al., 2012, in Ground-based and Airborne Instrumentation for Astronomy IV. p. 844630, doi:10.1117/12.926697
- Triaud A. H. M. J., et al., 2010, *A&A*, **524**, A25
- Triaud A. H. M. J., et al., 2011, *A&A*, **531**, A24
- Weidenschilling S. J., Marzari F., 1996, *Nature*, **384**, 619
- West A. A., Weisenburger K. L., Irwin J., Berta-Thompson Z. K., Charbonneau D., Dittmann J., Pineda J. S., 2015, *ApJ*, **812**, 3
- Wu Y., Murray N., 2003, *ApJ*, **589**, 605
- de Wit J., Seager S., 2013, *Science*, **342**, 1473
- de Wit J., et al., 2016, preprint, ([arXiv:1606.01103](https://arxiv.org/abs/1606.01103))

Table 1. Adopted Stellar and Planet Parameters for the TRAPPIST-1 Planetary System.

Parameter	Value			Reference
TRAPPIST-1				
Stellar mass, M_s	$0.080 \pm 0.009 M_\odot$			Gillon et al. (2016)
Stellar radius, R_s	$0.117 \pm 0.004 R_\odot$			Gillon et al. (2016)
Project rotation velocity, $v \sin i_s$	$6 \pm 2 \text{ km s}^{-1}$			Reiners & Basri (2010)
Rotation period, P_{rot}	$1.40 \pm 0.05 \text{ days}$			Gillon et al. (2016)
Linear limb-darkening coefficient, u_1^a	0.021			Claret & Bloemen (2011) Eastman et al. (2013)
Quadratic limb-darkening coefficient, u_2^a	0.376			Claret & Bloemen (2011) Eastman et al. (2013)
	TRAPPIST-1b	TRAPPIST-1c	TRAPPIST-1d	
Orbital period, P (days)	1.510848	2.421848	18.20200	Gillon et al. (2016)
Time of mid-transit, T_0 (BJD)	2457322.51765	2457362.80520	2457294.7744	Gillon et al. (2016)
Planetary radius, r_p (R_\oplus)	1.113	1.049	1.163	Gillon et al. (2016)
(assumed) Planetary mass, m_p (M_\oplus)	1.379	1.154	1.573	This work
Eccentricity, e	0	0	0	Gillon et al. (2016)
Inclination, i_p (deg)	89.410	89.488	89.893	Gillon et al. (2016)
Impact parameter, b (R_s)	0.21	0.25	0.24	Gillon et al. (2016)
(expected) Doppler semi-amplitude, K_{Dop} (m s^{-1})	4.136	2.959	2.059	This work
(expected) Rossiter-McLaughlin semi-amplitude, K_{RM} (m s^{-1})	45.909	40.747	50.162	This work

^a Obtained from the interpolation over the grid of quadratic limb-darkening coefficients from Claret & Bloemen (2011) in the J-band. For the star we assume $T_{\text{eff}} = 2550 \text{ K}$, $[\text{Fe}/\text{H}] = 0.04 \text{ dex}$, and $\log g = 5.2 \text{ (cgs)}$ (Gillon et al. 2016).

This paper has been typeset from a $\text{T}_\text{E}\text{X}/\text{L}^\text{A}\text{T}_\text{E}\text{X}$ file prepared by the author.